Cluster Assembly Dynamics Drive Fidelity of Planar Cell Polarity Polarization

AUTHORS

Silas Boye Nissen[1,2,3], Alexis T. Weiner[1], Kaye Suyama[1], Pablo Sanchez Bosch[1], Song Song[1], Yuan Gu[4], Alexander R. Dunn[3,5], Jeffrey D. Axelrod[1,5]

1 Department of Pathology, Stanford University School of Medicine, Stanford, CA, USA

2 The Novo Nordisk Foundation Center for Stem Cell Medicine (reNEW), University of Copenhagen, Copenhagen, Denmark

3 Department of Chemical Engineering, Stanford University, Stanford, CA, USA

4 Quantitative Science Unit, Stanford University School of Medicine, Stanford, CA, USA

5 These authors contributed equally

ABSTRACT

The planar cell polarity (PCP) signaling pathway polarizes epithelial cells in the tissue plane by segregating distinct molecular subcomplexes to opposite sides of each cell, where they interact across intercellular junctions to form asymmetric clusters. The role of clustering in this process is unknown. We hypothesized that protein cluster size distributions could be used to infer the underlying molecular dynamics and function of cluster assembly and polarization. We developed a method to count the number of monomers of core PCP proteins within individual clusters in live animals, and made measurements over time and space in wild type and in strategically chosen mutants. The data demonstrate that clustering is required for polarization, and together with mathematical modeling provide evidence that cluster assembly dynamics dictate that larger clusters are more likely to be strongly asymmetric and correctly oriented. We propose that cluster assembly dynamics thereby drive fidelity of cell- and tissue-level polarization.

INTRODUCTION

The assembly of proteins into large, complex assemblies is a ubiquitous aspect of both signal transduction cascades and the protein complexes that mediate adhesion between neighboring cells[1]. These structures have features in common with biological condensates such as large and variable sizes and complex stoichiometries[2]. In general, the functions of cluster formation are still incompletely understood. This knowledge gap reflects, in part, the considerable difficulty in understanding how these large protein assemblies form, and how their formation relates to function.

Building on an established theoretical framework[3], biologists have used protein cluster size distributions to infer their underlying assembly dynamics. The E-Cadherin cluster size distribution in the *Drosophila* embryonic epithelium was found to obey a power law distribution with exponential decay limiting the largest sizes[4]. From this, it was inferred that cluster assembly is regulated by a combination of fusion and fission, along with the selective removal of large clusters. In another example, an exponential size distribution for clusters of the scaffolding protein PAR-3 was found in *C. elegans*[5]. Together with additional experimental evidence, this led to the proposal that two positive feedback mechanisms stabilize the asymmetric distribution of PAR-3[6,7].

In planar cell polarity (PCP) signaling, the six core components, Flamingo (Fmi)[8,9], Frizzled (Fz)[10,11], Van Gogh (Vang)[12,13], Dishevelled (Dsh)[14,15], Diego (Dgo)[16], and Prickle (Pk)[17] break cellular symmetry by segregating distinct subcomplexes to opposite sides of the cell[18]. The two subcomplexes communicate intercellularly, recruiting one subcomplex (Fmi-Fz-Dsh-Dgo) to one side of the cell junction, and the other subcomplex (Fmi-Vang-Pk) to the opposite side. In *Drosophila* wing cells, the two oppositely localized subcomplexes direct cytoskeletal regulators to orient the growth of pre-hairs[19,20,21]. In vertebrates, including humans, PCP is essential for a variety of developmental processes, for example neural tube closure and heart formation, and for several physiological and pathological processes such as wound healing and cancer invasion[18].

The observed behavior of the core PCP system, combined with mathematical modeling, suggests that it acts as a bistable switch, breaking symmetry to produce a stable, polarized array[22-25]. Furthermore, the formation and segregation of PCP subcomplexes is associated with assembly of the components into clusters[26,27]. Why this is so is not understood. We hypothesized that elucidating the PCP cluster size distribution would yield insight into the underlying functional importance of clusters in PCP signaling.

Construction of the core PCP complex Dgo-Dsh-Fz-Fmi=Fmi-Vang-Pk (Fig 1a) that spans intercellular junctions (indicated by =) was proposed to initially involve assembly of the transmembrane components into an asymmetric bridge comprising Fz-Fmi=Fmi-Vang[28]. Addition of the cytoplasmic components (Dgo, Dsh, and Pk) forms a complete, asymmetric complex (with asymmetry here defined as unequal amounts of Fz, Dgo, Dsh, Vang and/or Pk on the two sides of the complex). A critical element of this model is a preferential asymmetry, such that Fz-Fmi=Fmi-Vang is preferred over symmetric Fz-Fmi=Fmi-Fz or Vang-Fmi=Fmi-Vang[29]. A minimal Fz-Fmi=Fmi-Vang bridge can transmit polarity information between cells without the cytoplasmic factors Dsh, Dgo, and Pk, for example, when Fz or Vang is clonally overexpressed[28]. However, these cytoplasmic factors are required for the acquisition of cell polarization when Fz and Vang are expressed at their endogenous levels. While it is well established that asymmetric signaling is transmitted between cells by Fmi=Fmi bridges[28-32], the basis for creating the underlying asymmetry is not certain. Functional evidence from our prior work indicates that the association of Fz with Fmi modifies the nature of the information it signals to the adjacent cell[29]. By whatever mechanism, the presence of Fz on one side of the bridge promotes Vang on the opposite side, and vice versa.

In confocal images, asymmetry appears to be greatest in junctional regions containing clusters of PCP complexes, which appear as bright puncta[26,27]. This observation suggests that 'mutual exclusion', wherein proximal and distal subcomplexes exclude each other from their respective domains[18], is somehow associated with cluster formation. PCP clusters are inferred to contain all six core components, and cluster formation is likely mediated by a number of previously observed phenomena. Overexpression of Dsh or Pk results in the formation of huge puncta[16,33,34], and in the absence of either protein, the size and stability of puncta are diminished[26,27]. Oligomerization may contribute to clustering, as the DIX domain in Dsh and a poorly characterized domain in Pk mediate oligomerization[35,36]. N-terminal Vang phosphorylation sites appear to modulate clustering[35,37,38] and Fmi *cis*-interactions may promote clustering[39-41]. Clustering may be associated with stability: the localization of Fmi and Fz within large puncta is more stable than elsewhere, as judged by fluorescence recovery after photobleaching (FRAP)[27]. Surprisingly, the stoichiometry of complexes is not fixed: semiquantitative imaging revealed that modest changes in expression levels of any cytoplasmic components altered their incorporation into complexes without changing the relative abundance other components[42].

Whether cluster formation in PCP signaling is functionally significant, and if so, in what way, is unknown. For example, cluster size might be related to asymmetry (defined as above), proper orientation (in the wing, defined as Fz, Dgo and Dsh accumulating on the distal side and Vang and Pk accumulating on the proximal side of cells), or to the ability to transduce a downstream response. To address this question, we developed a method to quantify the number of monomers of the core PCP proteins within individual complexes, thereby defining distributions and relationships in various wild-type and mutant conditions, including in mutants that specifically impair clustering. We then captured these measurements, prior knowledge, and data from Weiner et al.[43] (companion manuscript) to suggest a mathematical model of cluster formation and a mechanism for symmetry breaking. From these studies, we draw an overarching conclusion that growth of sufficiently large clusters is necessary for cell polarization; we suggest that the asymmetry of individual clusters and the probability of correct cluster orientation increase with size, and we propose that this fidelity mechanism is driven by cluster assembly dynamics.

RESULTS

The core PCP signaling proteins assemble into clusters that follow a size-independent growth mechanism

We hypothesized that quantifying the distribution of PCP cluster sizes would yield insight into how clusters grow, and that carefully defining cluster composition could provide insight into how symmetry breaking occurs. Among many possibilities for growth, clusters may grow to a fixed, uniform, cluster size distribution where the on- and off-rates equilibrate, perhaps reflecting a scaffolding effect. Alternatively, clusters might undergo coarsening, continually fusing to result in non-stable bimodal cluster size distribution at intermediate time points and a single large cluster at steady state (presumably not reached), or a combination of fusion and fission might yield a power law distribution[44]. Furthermore, the bistability proposed as a central feature of PCP signaling[22] might be encoded in a cooperative mechanism resulting in nonlinear cluster growth, *i.e.* positive feedback in the recruitment of individual components into clusters. None of these possibilities have been examined to our knowledge.

For quantification, we employed eGFP-tagged core PCP proteins previously validated to express and incorporate into clusters at levels similar to the endogenous proteins (except for the Fz::eGFP probe that incorporates more efficiently than endogenous Fz; no correction for this effect is made in the present analyses)[42]. Imaging at high spatial resolution in live tissue by TIRF microscopy, we observe many more clusters of varying sizes than previously appreciated (Fig. 1B). To obtain cluster size distributions, we count the number of fluorophores in each cluster by identifying fluorophore steps in the bleaching trace (see Methods).

For each of the six core proteins, at proximal-distal (P-D) boundaries, the molecular size distributions we observed are well fit by single exponential functions (Fig. 1C-H; see Methods). These data are inconsistent with models that predict uniform cluster sizes, coarsening (fusion), or a combination of fission and fusion. Consistent with prior results[27], imaging over several hours shows little mobility of clusters (Movie S1), again indicating that cluster fission and fusion are rare. Instead, exponential cluster size distributions are parsimoniously explained by cluster growth and decay rates independent of the cluster size, with decay rates necessarily higher than the corresponding growth rates[45]. Importantly, the exponential cluster size distributions indicate that bistability proposed to underlie PCP asymmetry is not a consequence of cooperative recruitment of any one component to individual clusters.

We also observe exponential cluster size distributions at anterior-posterior (A-P) boundaries, though with smaller average sizes for each protein, consistent with the lower signal seen there in lower resolution confocal images (Fig. S1).

Clusters grow and cluster stoichiometry is maintained

To determine whether cluster size distribution evolves as cellular asymmetry (the segregation of Fz, Dgo, Dsh, from Vang, Pk within a cell) increases, we measured the evolution of cluster stoichiometry and size over time. A wave of cell divisions and a dramatic reorganization of microtubules between 14 and 16 hrs after puparium formation (APF)[46] disturb PCP, allowing us to assay cluster composition as cellular polarity is consolidating following this disturbance. At P-D boundaries, the number of each molecule within clusters grows between 15 and 32 hrs APF. (Fig. 2). In contrast to the growth of clusters over time at P-D boundaries, we see no or little growth of clusters at A-P boundaries (Fig. S2). Our results for P-D boundaries differ modestly from previous estimates that found no growth of any component except for a very small growth of Vang between 20 and 28 hr APF, perhaps because the prior study was only able to visualize and assay the largest clusters[42].

We estimated average numbers of components within individual clusters at 23.5 hr APF (Fig. 2). This result equates to an approximate stoichiometry of 2:4:1:1:1:1 for Fmi, Vang, Fz, Dgo, Dsh, Pk respectively. We note that this is an average, and it does not necessarily reflect the stoichiometry of individual clusters (see below). The number of monomers of the six proteins in clusters grow at rates that would maintain roughly the same stoichiometry during the 15 to 32 hr interval studied (Fig. 2).

The density of clusters for each protein along any membrane remained roughly the same and independent of age (not shown), and live imaging showed minimal mobility of clusters (Movie S1). Taken together, these observations suggest that clusters undergo growth and decay for the most part independently of each other.

Clonal analysis reveals that a population of distal Vang is present in PCP clusters

To determine how polarized each component is within individual clusters, we separately counted the number of molecules in proximal and distal subcomplexes using clonally expressed probes. All the resulting cluster size distributions again followed single-exponential distributions (Fig. S3). For Fmi, these data reveal equivalent size distributions (and numbers of clusters) on the proximal and distal sides of junctions with an average of 5 Fmi monomers on each side at 23.5 h APF (Fig. 3A,A',A''), consistent with a 1:1 *trans* homodimer configuration. The number of Fmi monomers on either side increases with an average addition of one monomer every 2-3 hours.

In contrast, Fz is highly polarized with most on the distal side and very little on the proximal side (Fig. 3B,B',B''). Fz was found in similar numbers on the distal side as Fmi, suggesting a roughly 1:1 stoichiometry between the two proteins on the distal side. The distal Fz population grows at the same speed as Fmi, one monomer every three hours on average, maintaining 1:1 stoichiometry (As noted above, the actual ratio in wild-type animals may be somewhat lower as the Fz probe incorporates more efficiently than endogenous Fz.) In contrast, proximal Fz also exists in a single exponential distribution (Fig. S3B'), but with an average size of only single monomers per cluster and does not change with age.

Pk behaves essentially as a mirror image of Fz (Fig. 3C,C',C''). On the proximal side, clusters were of average size 9 at 23.5 h APF and grow at a rate equivalent to that of distal Fz and Fmi.

Distal Pk exists on average as single monomers and does not grow with age. We infer that many clusters have no Fz and Pk on the 'wrong' side based on the low density of monomers and larger clusters observed.

Proximal Vang exists in numbers larger than any other core protein (Fig. 3D,D''): three-fold higher than proximal Pk and five-fold higher than proximal Fmi. Proximal Vang grows at 3 monomers every 2-3 hours, maintaining the 1:3 Pk:Vang stoichiometry on the proximal side. Surprisingly, we find a significant population of Vang on the distal side (visible in Fig. 3D and quantified in Fig. 3D'), with an average distal subcomplex containing 3 Vang monomers (Fig. 2E). The distal Vang population is smaller than both distal Fmi, and distal Fz, but 3-fold larger than distal Pk. This finding was not anticipated based on prevailing understanding, although it was evident but not commented upon in an earlier report[26]. We find a slow but significant growth in the distal Vang population with 1 monomer being added every 5 hours on average. Thus, growth in the number of Vang molecules occurs primarily on the proximal side, and at 30 hours, when the position of pre-hair growth is set, and cell polarization appears strongest, large clusters with large amounts of proximal Vang are present.

In sum, equal amounts of Fmi are present on the distal and proximal sides, whereas Fz, Pk, and Vang are roughly 90% polarized, with Vang present at an approximately three- to four-fold excess over Pk.

Clusters form in null mutants

Null mutants of each core protein produce substantial polarity defects and inhibit asymmetric distribution of other core proteins, indicating that PCP is profoundly compromised at a functional level. Multiple interactions between core components have been reported[18], and data suggest that several core proteins can oligomerize[35-41], consistent with the possibility that clustering might not require the presence of the full complement of components. However, the extent to which clusters might form in the absence of any individual core PCP protein has not been quantitatively assessed.

We used molecular counting to determine how cluster assembly is altered in the absence of individual core proteins. For all loss-of-function condition examined, we observe clusters (Fig. S4). In *fz* mutants, Fmi forms clusters of similar size to wild-type at early time points, suggesting that Fmi incorporated into PCP clusters does not depend on Fz (Fig. 4A-A''). However, in the absence of Fz, subsequent growth of Fmi in clusters does not occur. Similarly, in *fz* mutants, both Vang and Pk are recruited into clusters at levels comparable to wild-type at early time points (Fig. 4B-C''). As with Fmi, Vang and Pk levels fail to grow. This dependency suggests that a Fz-dependent signal from the distal side increases the recruitment rate of proximal Vang but is not required for its baseline recruitment (We show below that this signal depends not only on Fz but also on Dsh.) Conversely, quantifying *vang* or *pk* mutants revealed that the number of Fz molecules within early clusters does not depend on the presence of Vang or Pk; however, growth of Fz levels does depend on both Vang and Pk, suggesting that a Vang-dependent signal from the proximal side increases the recruitment rate of distal Fz (Fig. 4D-E''; see also ref. [47]). Thus, the stoichiometry of the core proteins in clusters differed between wild type and null mutants, where we find roughly equal numbers of monomers of each protein with slightly more Vang.

Importantly, we did not measure a failure to form clusters in any null mutant condition examined, though we cannot rule out that unmeasured proteins were not recruited to clusters for a given null mutant. As discussed in the companion study, the observations that cells lacking Fmi retain the ability to polarize, and that both Fz and Vang cluster in those cells, imply both that some

level of cell-autonomous proximal and distal subcomplex formation occurs in the absence of Fmi and that these subcomplexes are competent to mediate feedback required for polarization[43]. Thus, cluster formation is robust to the absence of Fmi, Fz, Vang, and Pk, even though each is necessary for tissue-level polarization.

Growth of larger clusters is required for downstream signaling

Removal of Fz, Pk, or Vang does not eliminate clustering but instead inhibits cluster growth, thereby reducing the probability of achieving the largest clusters. As these mutants disrupt the segregation of proximal and distal complexes that define cellular asymmetry, we hypothesized that the assembly of larger clusters might be necessary to generate reliably polarized clusters and cells. However, in these mutants, other functions of the missing proteins might account for the failure to polarize. We therefore sought a way to disrupt clustering as precisely as possible while leaving other functions intact.

To do so, we leveraged a well-defined structure/function relationship. The DIX domain of Dsh is known to oligomerize and is thought to mediate Dsh clustering *in vivo*[35,48,49]. A previous study characterized an allelic series of single amino acid substitutions in mouse Dishevelled2 (Dvl2) that disrupt oligomerization to varying degrees by disrupting antiparallel inter-strand interactions[35]. Based on these data, we created orthologous *Drosophila* dsh^{DIX} point mutants expected to partially or entirely block Dsh oligomerization. Each, along with a wild-type control, was made on a transgene driven by the *Dsh* promoter and placed on a dsh^{v26} null chromosome. All three mutants express at levels similar to the wild type, and mediate sufficient Wingless (Wg) signaling to support some viability through pupal and adult stages.

Three mutants, Dsh^{N80D}, $Dsh^{N80A,}$ and Dsh^{G63D}, produce a range of polarity phenotypic strengths, with Dsh^{N80D} being the weakest, Dsh^{N80A} being stronger, and Dsh^{G63D} slightly stronger still (Fig. 5A-D). We assess that Dsh^{G63D} is the strongest because, while hemizygous males of each were viable, homozygous females of Dsh^{N80D} and Dsh^{N80A} were viable, but Dsh^{G63D} females were not, and Dsh^{G63D} male wings consistently display notches consistent with Wg signaling defects not seen in the Dsh^{N80D} and Dsh^{N80A} wings, suggesting a progressively stronger effect on the Wg pathway as well. Therefore, these mutants form an allelic series with respect to PCP phenotype that mirrors the previously observed effects of their Dvl analogs in an *in vitro* Wnt signaling assay[35].

To assess their impact on clustering, we introduced the Vang::eGFP probe into the three Dsh mutants. Viability limitations prevented us from creating flies with homozygous Vang::eGFP, so Vang::eGFP was instead used as a heterozygous probe, which allowed us to compare relative molecular counts. We observed that cluster formation still occurs in each mutant, but that Vang cluster size is reduced in each of the mutants relative to wild-type, with the extent of reduction roughly proportional to the strength of the polarity defect (Fig. 5A'-D'). Little or no cluster growth over time was observed, though our sensitivity for detecting growth with heterozygous probes was low, as little growth in the Dsh^{WT} control could be seen.

We introduced Fz::eGFP as a homozygous probe and counted it in the presence of Dsh^{N80A} and Dsh^{G63D} (Fig. 5A''-D''). Again, Fz is incorporated into clusters, though of modestly decreased size, and while growth appears to have occurred in the Dsh^{WT} control (see legend to Fig. 5), no growth over time was observed in the Dsh^{DIX} mutants.

We conclude that Dsh^{DIX} mutants that selectively impair oligomerization while leaving other functions of the Dsh protein intact allow PCP clusters to form but impair their ability to form larger clusters. These effects are proportional to their ability to mediate the core PCP function

across alleles of varying strength. These data are consistent with the hypothesis that acquisition of large cluster sizes is required to effectively create cluster, cellular and tissue asymmetry.

Two-color imaging reveals that the likelihood of correct cluster orientation increases with cluster size

Our analyses to this point determined the cluster size distributions of individual components. However, these assays could not reveal the degree to which the numbers of different components correlate within individual clusters. To do so, we created flies that uniformly express mScarlet::Vang plus Fmi::eGFP, Vang::eGFP plus Fz::mScarlet, and mScarlet::Vang plus Pk::eGFP (Fig. 6A-C). We then quantified the intensities of mScarlet and eGFP in each identifiable fluorescent punctum (Fig. 6A'-C'). (The dimness of mScarlet relative to eGFP did not permit molecular counting.) Despite the expected noise due to the limitations of this quantification approach, for each combination, there is rough proportionality, indicating that, at least for Vang, Fmi, Fz and Pk, smaller clusters are smaller for each component, and larger clusters are larger for each component when assessing the summed P-D boundaries. The modest correlation we observe is consistent with a variable stoichiometry, as previously proposed[42]. The same relationship holds true for the A-P clusters (Fig. S5).

Parsing our single-color counting results by comparing mosaics of P-D and A-P clusters provided a hint that larger clusters (P-D) are more asymmetric than smaller (A-P) ones. For Pk and Vang, cluster size measurements should be similar when comparing the proximal side to the sum of both sides, since within each cluster, most monomers are on the proximal side. The mirror argument applies for Fz. However, in a non-polarized cluster, as might occur at A-P boundaries, roughly equal amounts of Fz or Pk are predicted on both sides. In this case, the number of molecules counted at an A-P clone boundary should be roughly half of that counted when both sides are included. Indeed, whereas P-D boundaries labeled on the 'correct' side or both sides yielded roughly similar results, counting measurements at A-P clone boundaries show roughly half as many Fz, Pk or Vang molecules present as compared to A-P boundaries in which both sides are labeled (Table S1 and Fig. S2). Fmi, that is expected, by all measurements, to be symmetrical, confirms this trend. Though the values are small, the trend indicates that P-D boundaries are more asymmetric than are A-P boundaries, consistent with the idea that asymmetry increases with cluster size. Stronger evidence emerged from the following cluster-by-cluster two-color analysis.

Our observation of a distal Vang population was surprising (Fig. 3D-D'). Distal Vang could, in principle, reflect a previously unrecognized role for Vang in distal PCP clusters, the presence of clusters with reversed orientation, or Vang oligomers that are not associated with canonical PCP clusters. To further define this population, we applied the two-color quantification described above to clone boundaries. We began by asking if the distal Vang clusters are included in intercellular complexes or if they could form independent of the other core proteins. To address this question, we analyzed interfaces between twin clones expressing mScarlet::Vang and Fmi::eGFP in adjacent cells (Fig. 6D), thereby unambiguously identifying signal on proximal and distal sides of the junction. Where distal Vang was present, it was almost always accompanied by proximal Fmi, suggesting that distal Vang is associated with Fmi homodimers spanning the intercellular junction. Importantly, distal Vang was most often associated with small proximal Fmi clusters (Fig. 6D'). In contrast, per cluster, proximal Vang counts were roughly proportional to distal Fmi counts (Fig. 6D''). Numerous large proximal Fmi clusters were not associated with distal Vang, implying that not all intercellular complexes contain distal Vang. These data indicate that distal Vang tends to exist within small clusters, and that distal Vang tends to be excluded from larger clusters.

We further explored the composition of distal Vang-containing clusters by asking whether distal Fz accompanies distal Vang. Imaging Vang::eGFP clones in a uniform Fz::mScarlet background (Fig. 6E), we see that most distal Vang colocalizes with Fz. Since almost all Fz was found to be on the distal side (Fig. 3B,B',B''), we infer that at least some distal Vang exists in clusters with distal Fz. Importantly, the amount of distal Vang anticorrelates with the amount of Fz (Fig. 6E''), confirming that distal Vang tends to be excluded from large clusters. Not surprisingly, as a control, we find that proximal Vang correlates with uniform Fz (Fig. 6E'). We similarly assayed the relationship between distal Vang and proximal Pk (Fig. 6F). At interfaces of twin clones expressing mScarlet::Vang and Pk::eGFP, we again see that the amount of distal Vang anticorrelates with the amount of proximal Pk (Fig. 6F'). These results suggest that the largest, though still relatively small, clusters containing distal Vang may be asymmetrical clusters oriented the wrong way, and clusters with somewhat less distal Vang can contain larger numbers of distal Fz and proximal Vang. The largest Fz-containing clusters have very little, if any, distal Vang.

We interpret these results to indicate that small clusters can be oriented incorrectly, but during cluster growth, distal Vang and distal Pk are excluded and distal Fz and proximal Pk accumulate, such that the clusters that grow largest are most likely to be correctly oriented. If this is correct, we would expect the number of proximal Vang monomers to correlate with the number of Fz monomers, and this is indeed observed (Fig. 6D'). These relationships are probably stochastic, and it is likely true that some correctly polarized larger clusters containing distal Fz and proximal Pk (and, by inference, proximal Vang) also contain some amount of distal Vang; the companion manuscript proposes consequences of the presence of distal Vang[43] (see Discussion).

We note that this method only pairs clusters with a detected signal in both channels in close proximity to each other. It does not quantify intensities inside clusters that do not have a detected partner in the other channel. Including unmatched clusters is not expected to qualitatively change the results. The reported anticorrelations should still hold true, and including unmatched clusters would only strengthen that trend.

Together, our two-color measurements suggest that cluster assembly dynamics underlie the fidelity of cluster polarization and orientation: as clusters enlarge, they are less likely to have distal Vang and more likely to accumulate proximal Vang thus being properly oriented.

Mathematical model of cluster formation

The above measurements and known relationships constrain possible models of cluster formation, growth, and asymmetry. Previous mathematical models of PCP have not explicitly considered clustering in this process. We tested whether a relatively simple set of molecular interactions could explain the phenomena we measured experimentally. After exploring multiple possibilities, we arrived at a mathematical model in which clusters grow and shrink stochastically and independently of each other. We first describe a simplified 2-component version consisting of the subcomplexes *F* and *V* that mutually inhibit each other intracellularly (factor δ)[26,26,50]. In this framework (Fig. 7A), *F* is the number of subcomplexes within a cluster consisting of Fz-Dgo-Dsh. Similarly, *V* is the number of subcomplexes consisting of Pk-Vang. Note that *F* and *V* can be recruited to both distal and proximal sides of clusters, and they communicate across the junction through a factor γ (mediated by Fmi).

The model excludes cluster fission and fusion and describes the stochastic evolution of individual clusters (Fig. 7B). Since we do not find any limits to the size of a cluster, we assume a well-mixed, non-limiting population of free monomers. We do not distinguish between free

monomers at the membrane vs free monomers inside the cytoplasm. All *F* and *V* subcomplexes enter or leave the cluster according to equations 5-8 (see Methods). We model an influx bias ($\alpha > \beta$) that acts on *F* based on previous findings that Fz and Dsh are transported away from the proximal side and toward the distal side[51-53], thereby breaking cluster symmetry. The off rate must be larger than the on rate to eliminate runaway cluster growth ($\alpha < 0.5$). We do not implement any self-promotion or -inhibition of *F* or *V* (i.e., the probability of adding or subtracting *F* or *V* is independent of the amount already in the cluster) since doing so would result in non-exponential cluster size distributions.

This simplified model replicates key experimental findings and illuminates how the model variables contribute to phenotypes. Exponential cluster size distributions and asymmetry in clusters is reproduced (Fig. 7C), where the fraction of *V* or *F* on the incorrect side is primarily determined by β and γ, while the amount on the correct side, and therefore the overall size of clusters, is determined mainly by α (Fig. S6). Setting γ and δ to zero isolates *V* and *F* from each other, simulating a null mutant; this eliminates asymmetry while preserving the exponential distribution of the remaining component (compare Fig. 7C to Fig. 3). If one assumes that Dsh^{DIX} mutants diminish the ability of components to oligomerize to build complexes, one can approximate this condition in simulation by decreasing α; modestly reducing α causes cluster size to shrink and asymmetry to be reduced, as is seen experimentally (Fig. S7, and compare Fig. S6 to Fig. 5). In contrast to the influx bias at P-D boundaries, A-P boundaries are not subject to this asymmetry and would therefore remain symmetric. Setting $\beta = \alpha$ simulates this condition and results in symmetric clusters on the population level (Figs. S6-S7). Interestingly, as δ gets stronger, the size of complexes decreases, but if δ goes to zero, *F* will polarize but *V* will not polarize at all (Fig. S6). Therefore, it is likely that a moderate level of mutual inhibition occurs *in vivo*. Finally, in the companion manuscript, we show the surprising result that individual cells lacking Fmi, as well as cells expressing a truncated Fmi that cannot form *trans* dimers, still polarize. Modeling this condition by setting $\gamma = 0$ while keeping $\delta > 0$ predicts that cells still polarize, though less strongly than in wild-type (Fig. 7E and Fig. S7). A distillation of these results can be visualized in a phase plot (Fig. 7E). The ability of our model to capture conditions examined here and elsewhere demonstrates the ability of this reduced model to represent the underlying biology.

The model makes the important predictions that the probability of correct orientation increases with cluster size in a non-linear fashion (Fig. 7F), and that large clusters are predicted, on average, to be more asymmetric than smaller clusters (Fig. 7D). Both of these predictions are consistent with our two-color measurements (Fig. 6D'',E') and with the comparison between P-D and A-P boundaries (Table 1). Increased fidelity in cluster polarization with cluster growth, and decreased probability of reversed polarization would both be expected to produce a more coherent signal to downstream effectors (see Discussion).

While considerable insight can be derived from this simplified mathematical model, a more complex version can be used to describe the behavior of individual proteins rather than *V* and *F* subcomplexes, demonstrating the feasibility of stochastic unordered addition and subtraction of monomers, and of the various interactions modeled by the equations to reflect the underlying biology (see Appendix, Fig. S8, and Movie S2). Furthermore, additional features could be incorporated to capture additional behaviors. For example, the potential effects of limiting pools of one or more free components could be considered, and insight re timescales might derive from measuring the average lifetime of a cluster.

DISCUSSION

Our measurements allow us to draw several detailed mechanistic conclusions: ***i)*** Exponential distributions of cluster sizes for all six core proteins suggest that the on- and off-rates for each are independent of the cluster size; ***ii)*** a previously unrecognized population of distal Vang is identified, which, together with data from the companion manuscript[43], leads us to a model for symmetry breaking; ***iii)*** clustering is observed in all null mutants examined, consistent with the multiple oligomerization and intermolecular interactions so far identified; ***iv)*** a specific oligomerization mutant reveals that growth of larger clusters is required to achieve cell polarization; ***v)*** that as clusters grow in size, they become increasingly polarized and increasingly likely to be correctly oriented. These findings led us to propose a dynamical model for PCP cluster assembly that incorporates each core protein stochastically, and that multiple cluster assembly trajectories lead from small, randomly oriented, clusters to large, highly asymmetric, correctly oriented, clusters. The interactions described by this model allow the PCP pathway to produce a reliably polarized output despite a weak biasing input.

Single exponential distributions imply that the probability of a monomer of any core protein entering or leaving a cluster is independent of the number of monomers in the cluster, and that the off rate must be larger than the on rate[45]. Although clusters are on average 3-4-fold larger along P-D boundaries compared to along A-P boundaries, clusters along both boundaries form single exponential size distributions (Fig. 1 and S1). Multiple models for cluster growth, such as fixed scaffolding, fission and fusion, and coarsening, are inconsistent with the observed exponential distributions[4,44]. Furthermore, our results do not provide evidence for cooperative recruitment of individual components that might produce bistability in the system. One possibility is that clusters behave as filaments to which monomers can be added or subtracted only from one or both ends. The behavior of actin and microtubule filaments has been modeled and shown to predict exponential distributions[54,55]. Exponential distributions can also arise in systems undergoing coagulation[56], but observations of little fusion of PCP clusters on a timescale of hours suggests this is an unlikely mechanism of clustering in PCP. Structural studies of PCP clusters will be required to test the filament hypothesis.

Prior analyses evaluated the stoichiometry and stable fraction of core proteins in “puncta” and “non-puncta” identified by confocal microscopy[27,42]. It is now evident that much of the “non-puncta” consists of smaller puncta, previously acknowledged as a possibility[27], and likely also freely diffusing membrane-associated monomers. In that work, the stoichiometries of Fmi and Fz were said to be similar in “puncta” and “non-puncta,” while stable portions as assessed by fluorescence recovery after photobleaching (FRAP) were assessed as smaller in “non-puncta.” Reinterpreting these data, we suggest it is possible that the stable fraction in smaller, non-resolved, puncta could be similar to that in large puncta, and the measured lower stability could come from the higher proportion of freely diffusing monomers in the “non-puncta” regions. Similar stabilities in large and small puncta would be more consonant with our mathematical model.

Beyond limiting possible models of cluster growth, the counting measurements reported here provide additional insights into the mechanisms of cluster assembly and symmetry breaking. Our experimental results are replicated in model simulations that do not assume a fixed order of component addition to growing clusters. Importantly, in the companion manuscript, we observe clusters of Vang and clusters of Fz in cells expressing no Fmi, and indeed these cells polarize, falsifying the assumption that Fmi is an obligatory scaffold for complex formation[43]. Live-cell imaging likewise indicates that the initiation and evolution of each cluster likely occur independently, as we observe no obvious interactions between clusters on a time scale of hours (Movie S1). Whether clusters are seeded at yet unidentified spatial landmarks or if they seed randomly remains to be determined.

We report the surprising observation that a substantial population of Vang molecules exist in distal clusters (Fig. 3D-D'). Distal Vang colocalizes with Fz, as observed in two-color images (Fig. 6E-E''). The function of distal Vang, if it has any, is unknown. In the companion manuscript, it is shown that Vang associated with Fz has the propensity to recruit Pk, but that the recruitment of Dsh to those clusters inhibits Pk recruitment[43]. A parsimonious explanation is that the presence of distal Vang reflects the dynamics of cluster assembly, and that any consequence of its presence is inhibited by Dsh blocking its ability to recruit Pk. The amount of proximal Pk and distal Vang in a population of clusters do not correlate, suggesting that as clusters enlarge, acquiring more proximal Pk (and presumably distal Fz), distal Vang is more likely to be removed. This is discussed in more detail in Weiner et al.[43]

We measure a statistically significant increase in the number of all six core proteins in puncta along P-D boundaries from 15 to 32 hr APF (Fig. 2), and a larger growth of proximal Vang relative to the others (Fig. 3), consistent with, though much larger than, the growth of Vang previously reported between 20 and 28 hr APF[42]. Our results do not distinguish between the possibility that the growth in P-D clusters over time reflects not having reached steady state or if one or more parameters determining cluster dynamics are changing over time.

More broadly, we hypothesized that the growth of larger clusters is necessary for PCP signaling. To test this hypothesis, we used a series of mutations in the Dsh DIX oligomerization domain to tune the contribution of Dsh to cluster growth. These three mutants decreased cluster size proportionately to their polarity phenotypes (Fig. 5), providing evidence that larger average clusters are required for PCP signaling. This did not answer the question, however, as to why larger clusters are necessary and how these clusters are read out.

Several non-exclusive models might explain the need for large cluster formation in PCP signaling. First, large clusters may form more effective and more stable scaffolds to signal downstream events. In this case, even well-polarized smaller clusters would be ineffective in transducing a polarity signal. Second, our mathematical model predicts that larger clusters have a higher probability of orienting correctly. Third, smaller clusters are expected to be of mixed orientation and might, therefore, produce a less coherent signal. In contrast, larger clusters might have a higher probability of strong asymmetry than do smaller ones. The latter two relationships are captured in our mathematical model (Fig. 7) and observed in our 2-color experimental results (Fig. 6).

The simplified mathematical model replicates our key experimental observations, suggesting that it may capture the key features of PCP cluster growth and polarization. Notably, our data (and to our knowledge, literature observations) can be accounted for using only mutual inhibition between proximal and distal components and provide no evidence for the presence of positive feedback in the recruitment of individual components to growing clusters. As noted above, our data and the resulting model are consistent with the parsimonious interpretation that there is no set order or stoichiometry for the addition of components to PCP clusters. Finally and perhaps most importantly, our study provides compelling evidence for the hypothesis that cluster growth provides a simple but highly effective mechanism of error correction that can amplify modest biases in Fz and Dsh trafficking into highly efficient polarization. At a conceptual level, cluster growth thus provides a powerful means of amplifying weak and noisy inputs into a robust cellular output, in this case cell and tissue-level polarization.

METHODS

To determine how PCP clusters break symmetry, we developed a quantitative method to count the number of each of the six core proteins in individual PCP clusters. By analyzing bleaching

traces obtained with a high frame rate in live *Drosophila* wing cells imaged using total internal reflection microscopy (TIRF), we quantified the intensity of single fluorophores in each punctum and calculated the molecular number in the corresponding PCP cluster.

Genotypes

Wild type uniform expression experiments

Figs. 1C, 2A, S1A, S2A: w; P[acman]-eGFP::Dgo, FRT40A, dgo^{380}

Figs. 1D, 2B, S1B, S2B: yw, dsh^{V26}, FRT18; P[acman]-eGFP::Dsh

Figs. 1E, 2C, 4D', 4E', S1C, S2C (dark colors): w; +/+; Fz::eGFP

Figs. 1F, 2D, 4A', S1D, S2D (dark colors): w; Fmi::eGFP

Figs. 1G, 2E, 4B', S1E, S2E (dark colors): w; eGFP::Pk

Figs. 1B, 1H, 2F, 4C', S1F, S2F (dark colors), Movie S1: w; P[acman]-Stbm::eGFP, FRT40A, $Vang^{Stbm6}$ (P[acman]-Stbm::eGFP, a.k.a P[acman]-Vang::eGFP; ref [42])

Wild type clone boundary experiments

Figs. 3A-A'', S3A-A': UbxFLP; FRT42D Stan::eGFP / FRT42 arm-lacZ

Figs. 3B-B'', S3B-B': UbxFLP; arm-lacZ FRT73,80 / Fz::eGFP FRT80B

Figs. 3C-C'', S3C-C': UbxFLP; FRT42D eGFP::Pk / FRT42D arm-lacZ

Figs. 3D-D'', S3D-D': UbxFLP; P[acman]-Stbm, FRT40A, $Vang^{Stbm6}$ / P[acman]-Stbm::eGFP-LoxP, arm-lacZ, FRT40A, $Vang^{Stbm6}$

Loss-of-function uniformly labeled experiments

Figs. 4A,A'', S4A: w; Fmi::eGFP; Fz^{R52}

Figs. 4B,B'', S4B: FRT42D, pk::eGFP; Fz^{R52}

Figs. 4C,C'', S4C: P[acman]-Stbm::eGFP, FRT40A $Vang^{Stbm6}$; Fz^{R52}

Figs. 4D,D'', S4D: $Vang^{Stbm6}$; Fz::eGFP

Figs. 4E,E'', S4E: FRT42D, $pk^{pk\text{-}sple13}$; Fz::eGFP

Dsh[DIX] uniformly labeled experiments

Fig. 5A: Dsh-v5-6xmyc, $dsh^{V26,f36a}$

Fig. 5B: Dsh^{N80D}-v5-6xmyc, dsh^{V26}

Fig. 5C: Dsh^{N80A}-v5-6xmyc, dsh^{V26}

Fig. 5D: Dsh^{G63D}-v5-6xmyc, dsh^{V26}

Fig. 5A': Dsh-v5-6xmyc, $dsh^{V26,f36a}$; + / P[acman]-Stbm::eGFP, FRT40A, $Vang^{Stbm6}$

Fig. 5B': Dsh^{N80D}-v5-6xmyc, dsh^{V26}; + / P[acman]-Stbm::eGFP, FRT40A, $Vang^{Stbm6}$

Fig. 5C': Dsh^{N80A}-v5-6xmyc, dsh^{V26}; + / P[acman]-Stbm::eGFP, FRT40A, $Vang^{Stbm6}$

Fig. 5D': Dsh^{G63D}-v5-6xmyc, dsh^{V26}; + / P[acman]-Stbm::eGFP, FRT40A, Vang^{Stbm6}

Fig. 5A'': Dsh-v5-6xmyc, dsh^{V26,f36a}; Fz::eGFP

Fig. 5C'': Dsh^{N80A}-v5-6xmyc, dsh^{V26}; Fz::eGFP

Fig. 5D'': Dsh^{G63D}-v5-6xmyc, dsh^{V26}; Fz::eGFP

2-color experiments

Fig. 6A-A', S5A: hsFLP; P[acman]-Stbm,FRT40A,Vang^{Stbm6} / P[acman]-Stbm::eGFP,FRT40A, Vang^{Stbm6}; Fz::mScarlet (no heat-shock)

Fig. 6B-B', S5B: hsFLP; FRT42D,pk::eGFP / FRT42D,mScarlet::Vang, Vang^{Stbm6} (no heat-shock)

Fig. 6C-C', S5C: hsFLP; FRT42D,fmi::eGFP / FRT42D,mScarlet::Vang, Vang^{Stbm6} (no heat-shock)

Fig. 6D-D'': hsFLP; FRT42D,fmi::eGFP / FRT42D,mScarlet::Vang, Vang^{Stbm6} (12 min heat-shock)

Fig. 6E-E'': hsFLP; P[acman]-Stbm,FRT40A,Vang^{Stbm6} / P[acman]-Stbm::eGFP,FRT40A, Vang^{Stbm6}; Fz::mScarlet (12 min heat-shock)

Fig. 6F-F'': hsFLP; FRT42D,pk::eGFP / FRT42D,mScarlet::Vang, Vang^{Stbm6} (12 min heat-shock)

Sample preparation

Fly stocks were maintained on standard fly food. White pupae were selected at 0-3h after puparium formation (APF) and maintained at 25C until 15-32h APF. From each pupa, one wing sac was exposed by making a window in the pupal case[57,58]. A droplet of Halocarbon oil 700 (Sigma Life Science, refractive index 1.4, CAS No.: 9002-83-9) was placed on top of the exposed wing sac, and the wing was imaged at selected ages through a cover glass of thickness 1.5 (VWR Micro Cover Glass, selected 1 ounce, 18x18 mm, No. 1.5, VWR Cat No 48366-205).

Image acquisition

Live wings were imaged on an inverted total internal reflection fluorescence (TIRF) microscope (Nikon TiE) with an Apo TIRF 100x oil objective lens and numerical aperture 1.49 (see also refs.[59,60]). Distal eGFP expressing wing cells were located using low intensity (1%) 473-nm OBIS laser (Coherent). For 1-color experiments (eGFP), the exposed wing cells were fully bleached at high intensity (50%) laser power using the 473-nm OBIS laser and a sequential exposure of 50 ms. For 2-color experiments (mScarlet + eGFP), the exposed wing cells were first fully bleached using a 532-nm Crustalaser, and then fully bleached using the 473-nm OBIS laser. Both channels were acquired with 50 ms sequential exposure. An emission filter at 514/30nm (Semrock Inc.) was used for eGFP, and a 593/40nm filter (Semrock Inc.) was used for mScarlet. The images were recorded on a Hamamatsu Orca Flash 4.0 camera (fixed pixel size of 64 nm), and the scope was controlled using Micromanager[61] with Z-autofocus. The field of view varies from image to image due to variations in the wing area exposed. The number of frames acquired also varies from image to image due to variations in bleaching time needed, typically between 1,000 and 5,000 frames.

Image analysis

One image was selected per wing imaged. This image was selected based on the maximum number of cells in focus and xy drift less than 2px during image acquisition. No further drift correction was applied. These initial evaluation steps were performed in ImageJ[62]. All other post-processing steps were performed using custom-built MATLAB scripts. Cell boundaries, based on manually drawn nine px-wide masks were manually grouped into A-P and P-D boundaries for uniform expression wild type experiments and D, P, A or P for clone boundary wild type experiments. For mutant wing cells, all boundaries were assigned the same category. In the case of overlapping masks, P-D boundaries take precedence over A-P boundaries. For 2-color imaging, multi-modal image registration was performed based on the intensities in the first frame of each channel and applied on all frames of the mScarlet channel. Image transformation of the mScarlet channel was performed by integer xy pixel-translation only. No rotation, re-scaling, or shear were applied.

Locating clusters

For each image, the following steps were applied on all frames: to flatten the illumination and apply bleaching correction, a 2D Gaussian fit (2x2 pixels wide) was subtracted. To reduce camera pixel noise, the average intensity value within a moving box (3x3 pixels wide) was calculated. To minimize temporal noise, a directional moving median filter was calculated (with a maximum of 20 frames before and 0 frames after the current position). Then, to locate cluster centers inside the masked boundaries, local (5x5 pixels wide) maxima were identified. These pixel centers correspond to cluster centers.

Although we limit our counts to fluorophores inside manually masked membrane junctions (of width roughly 250 nm on either side of the junctions) and in a common z-plane, the method does not distinguish between monomers integrated into a cluster vs monomers that are not. We assume that highly mobile and therefore freely diffusing fluorophores account for a small fraction of identified counts, and that most fluorophores located in this way are incorporated into clusters. This places some constraints on the accuracy of our measurements that apply to both low density junctions (possibly overcounting monomers) and high-density junctions (possibly undercounting monomers hidden close to large bright clusters). Together, we expect these inaccuracies to minimally impact the final counts.

2-color intensities

To pair clusters in two different channels, the following approach was used on both channels: Inspired by the SRRF method[63], spatial resolution was increased by subdividing each pixel into 2x2 pixels in the xy direction and assigning the acquired value to the 4 subdivided pixels (new pixel size = 32x32 nm). Like the approach listed above, the illumination was flattened by subtracting a 2D Gaussian fit everywhere (5x5 pixels wide). Spatial noise was minimized by calculating the mean intensity value within a moving box (also 5x5 pixels wide). Temporal noise was reduced by determining the accumulated intensity inside each pixel during the first 5 frames. Cluster centers were located inside both channels independently by identifying local maxima (5x5 pixels). The processed intensity inside the center pixel of each cluster was dilated (6x6 pixels). Any uniquely overlapping dilated pixels across the two channels are said to correspond to a cluster containing the two labeled proteins.

Measuring cluster size

The following steps were applied for each cluster's pixel center: a histogram of the pair-wise difference is calculated for all frames to all future frames. The power spectrum is applied to this histogram, and the highest peak in the intensity interval between 40 and 110 is found. As internal validation, single fluorophore blinking events were found to occur within this interval. The highest peak indicates the most likely fluorophore intensity step size for that cluster. To estimate the number of fluorophores present in the first frame, the intensity of the first frame is divided by the local fluorophore step size and rounded down to the nearest integer. This counting method is inspired by refs. [64-66].

MATLAB image analysis scripts deposited at https://github.com/SilasBoyeNissen/Cluster-Assembly-Dynamics-Drive-Fidelity-of-Planar-Cell-Polarity-Polarization.

Statistical tests

For each wing, the average cluster size and its uncertainty are found by performing a non-linear regression model (a single exponential fit) on the experimentally found cluster size distribution. To assess whether the cluster size follows an exponential distribution, we used histograms and Q-Q plots for a visual inspection. The histogram of Vang::eGFP cluster size in the age interval 15-23h APF, for example, shows that the data (blue bars) closely follows the exponential density plot (red curve), indicating a good fit to an exponential distribution (Fig. S9A; data from Fig. 1). Similarly, the Q-Q plot for Dgo::eGFP cluster size in the age interval 24-32h APF demonstrates that the data points align well with the reference diagonal line, suggesting that the data matches the theoretical quantiles of an exponential distribution (Fig. S9B; data from Fig. 1). Together, these plots showed us that it is reasonable to assume the population distribution of cluster sizes for each wing follows an exponential distribution.

To test whether the average cluster size grows with age, a weighted linear regression model is performed on all wings with the same genotype. The mean value reported is now the predicted response of the linear regression model at 23.5h APF. The P-value reported is the t-statistic of the two-sided hypothesis test on the slope of the linear model. A P-value below 0.05 and a positive slope within error suggest that cluster size likely increases with age.

A linear mixed-effects model is used to test whether two genotypes have statistically different cluster sizes from each other. The model formula, Cluster size ~ age + genotype + age * genotype, evaluates the effects of age and genotype on cluster size, including their interaction. We report the P'-value for the genotype term. A P'-value below 0.05 indicates that the cluster sizes likely depend on the genotype.

pCas4-dsh-V5-6myc

The V5-6myc fragment, flanked by Xba1 sites, was generated by touch down PCR using pUAST-Rab35-6myc (Addgene #53503) as template.

Forward primer:
TCTAGAAGCGGCACAGGCTCTGGCGGCAAACCGATTCCGAACCCGCTGCTGGGCCTGGA
TAGCACCAGTGGTGGATCCACCATGGAGCAAAAGCTC

Reverse primer: TCTAGAATACCGGTGATTACAAGTCCTCTTC

pCas4-dsh from ref. [67] was digested with Xba1 and the V5-6xmyc fragment appended. The resulting plasmid was transformed into *w1118* flies to generate random genomic insertions, and an X chromosome insertion was recombined onto a *dshv26 f36a* chromosome.

DIX Domain Mutants

The pCas4-dsh-V5-6xmyc plasmid was mutated using TOPO Cloning to introduce conserved base changes analogous to those in Kan et. al.[35], resulting in N80D, N80A, and G63D mutations to the DIX domain. These three plasmids were then transformed into *w1118* flies to generate random genomic insertions, and an X chromosome insertion was recombined onto a *dshv26 f36a* chromosome. Parentheses indicate the analogous mouse mutation from Kan et al. (2020)[35].

A Zero Blunt TOPO Invitrogen kit introduced the following point mutations within the original pCasper4-dsh-V5-6myc plasmid.

G63D (G65D) F GCCGATTTCGATGTGGTCAAA. (GGT>GAT)

R GTCCATTGACTTGAAGAAGTAC

N80D (N82D) F GCCCTGCTTCGATGGGCGAGT. (AAT>GAT)

R AGTATGGTGGAGTCGTCGG

N80A (N82D) F GCCCTGCTTCGCTGGGCGAGT. (AAT>GCT)

R AGTATGGTGGAGTCGTCGG

PCR template pCasper4-dsh-V5-6myc (wild type control) with primers:

F GGCAGCGCTGGCAGTGTGACC.

R TCAGCACATCGCTGCTACTCG.

(Primers are outside Mlu1 and Xho1 digest sites.)

Individual Primer sets were used to introduce DIX point mutations via PCR into the original pCasper4-dsh-V5-6myc template, and these point mutations were inserted into the TOPO vector between the EcoR1 sites. Both the TOPO product (Dsh containing DIX mutation) and pCasper4-dsh-V5-6myc plasmid were digested using the Mlu1 and Xho restriction enzymes and the resulting fragments were then ligated together, resulting in pCasper4-dsh^{DIX}-V5-6xmyc. The prepared plasmid was sent to BestGene for injection. Random X insertions were recombined onto the *dsh^{V26}* chromosome.

Generation of mScarlet::Vang flies

We constructed the pBDP-mScarlet::Vang plasmid using Gibson assembly, with the NEB HiFi assembly kit. We used pBDP (https://www.addgene.org/17566/) as backbone. Vang 5', coding sequence (CDS), and 3' sequences were cloned from the BAC attB-P[acman]-AmpR-mApple-loxP-stbm (ref. [37]) mScarlet was obtained from pF3BGX-mScarlet (https://www.addgene.org/138391/). We integrated the mScarlet fragment after the Vang promoter region, right before the Vang CDS starting codon, followed by the linker sequence SGTGSG. We created the final plasmid using the following 5 PCR fragments:

Fragment 1: pBDP backbone. Primers: pBDP Fwd + pBDP Rev

Fragment 2: Vang 5'. Primers Vang5' Fwd + Vang5' Rev
Fragment 3: Linker-mScarlet. Primers Linker-mScarlet Fwd + Linker-mScarlet Rev
Fragment 5: Vang 3'. Primers Vang3' Fwd + Vang3' Rev

Primer sequences:

Primer name	Sequence
pBDP Fwd	CAGGTCTACGTGTTAGATCTTGGCCACGGGTGCGCATGATCGT
pBDP Rev	TTCAACCGCCAAACTGATAGGCGGCCGCGCGGGGATCCGG
Vang5' Fwd	CCGGATCCCCGCGCGGCCGCCTATCAGTTTGGCGGTTGAATTGCC
Vang5' Rev	GCCTCGCCCTTGCTCACCATTGCAATTGGGCTAGCGCGCG
Linker-mScarlet Fwd	CGCGCGCTAGCCCAATTGCAATGGTGAGCAAGGGCGAGGC
Linker-mScarlet Rev	ATGCCAGAGCCTGTGCCGCTCTTGTACAGCTCGTCCATGCC
Vang3' Fwd	AGAGCGGCACAGGCTCTGGCATGGAAAACGAATCCGTCAA
Vang3' Rev	ATCATGCGCACCCGTGGCCAAGATCTAACACGTAGACCTG

We inserted the plasmid using phiC31 into the attP landing site ZH-51C (BDSC #24482) and recombined it onto a *Vang*^{stbm6} (null) chromosome.

Math model

We introduce a Monte Carlo model consisting of two proteins (or, equivalently, protein subcomplexes), *F* and *V*, that can oligomerize on both sides, $_1$ and $_2$, of a cluster spanning a cell-cell junction. Thus, as an example, F_2 is the number of monomers of protein *F* inside cell 2 that is part of the cluster. The evolution, in real time units, *t'*, of the number of monomers of the two proteins in the cluster is described by the rate equations:

$$\frac{dF_1}{dt'} = \alpha' + \gamma'(V_2 - F_1) - \delta' V_1 - \tau' \quad (1)$$

$$\frac{dF_2}{dt'} = \beta' + \gamma'(V_1 - F_2) - \delta' V_2 - \tau' \quad (2)$$

$$\frac{dV_1}{dt'} = \alpha' + \gamma'(F_2 - V_1) - \delta' F_1 - \tau' \quad (3)$$

$$\frac{dV_2}{dt'} = \alpha' + \gamma'(F_1 - V_2) - \delta' F_2 - \tau' \quad (4)$$

where α' is the on rate of F_1, V_1, V_2, β' is the on rate of F_2, γ' is the intercellular coupling strength, δ' is the intracellular inhibition strength, and τ' is the off rate of both proteins on both side (see also Fig. 7A). These rate constants are unknown, and we assume they do not change with time nor are dependent on the state of the cluster.

We define a set of reduced rate constants $t=t'/c$, $\alpha=\alpha'/c$, $\beta=\beta'/c$, $\gamma=\gamma'/c$, $\delta=\delta'/c$, and $\tau=\tau'/c$ where $c=\alpha'+\tau'$, allowing us to reduce the rate equations to:

$$\frac{dF_1}{dt} = 2\alpha + \gamma(V_2 - F_1) - \delta V_1 - 1 \quad (5)$$

$$\frac{dF_2}{dt} = \beta + \gamma(V_1 - F_2) - \delta V_2 - 1 + \alpha \quad (6)$$

$$\frac{dV_1}{dt} = 2\alpha + \gamma(F_2 - V_1) - \delta F_1 - 1 \quad (7)$$

$$\frac{dV_2}{dt} = 2\alpha + \gamma(F_1 - V_2) - \delta F_2 - 1 \quad (8)$$

where t, α, β, γ, and δ are reduced time and rate constants in units of $\alpha' + \tau'$. β breaks the symmetry of the cluster when $\beta \neq \alpha$. Thereby, F can be considered an input protein that eventually breaks the symmetry of the output protein V when $\alpha \neq \beta$. To avoid infinite cluster growth, the off-rate (τ') is larger than the two on-rates (α' and β'). This condition implies that the number of monomers in the cluster performs a biased random walk towards 0 – the cluster is always about to collapse, and progressively larger clusters become exponentially less likely to occur. The parameter γ is the reduced intercellular coupling rate between the proteins in parenthesis. A value of $\gamma = 1$ implies a 1:1 stoichiometry between the proteins in question, whereas if $\gamma = 0$ the proteins in parenthesis are uncoupled and uncorrelated. The parameter δ is the reduced intracellular inhibition rate, which here increases linearly with the number of opposing monomers within the cluster. For $\delta = 0$, the growth of one protein is not inhibited by the opposing protein, whereas for $\delta = 1$, the inhibition is maximal.

Initially, for time $t = 0$, the cluster does not contain any monomers, meaning $F_1 = V_2 = F_2 = V_1 = 0$. We disallow protein of negative monomer numbers to occur, by setting the resulting decay rate to zero when no monomers are present. Otherwise, each following Gillespie model update stochastically selects a component to add or subtract one monomer based on the state of the cluster at that time. Thus, this model is a Markov process with no memory. The model runs as long as $t<T$ and is repeated for N independent clusters. The model is implemented in MATLAB, and the source code has been deposited at https://github.com/SilasBoyeNissen/Cluster-Assembly-Dynamics-Drive-Fidelity-of-Planar-Cell-Polarity-Polarization.

Conflict of interests

The authors declare that they have no conflict of interest.

Acknowledgments

We thank members of the Axelrod lab for fruitful discussions. Thanks to David Strutt for providing fly lines and the Stanford Research Computing Center for providing computational resources. We thank Claire Tomlin and James Ferrell for fruitful discussions on the mathematical model and William Weis for suggesting the point mutations in Dishevelled. Thanks to Alexandre Ravel for his support in the initial attempts to image the Dishevelled mutations. Stocks obtained from the Bloomington Drosophila Stock Center (NIH P40OD018537) were used in this study. This work was funded by NIH R35GM131914 (JDA), R35GM130332 (ARD), and NIH R01HL16929901 (JDA and ARD). SBN was supported by the Novo Nordisk Foundation (grant awards NNF20OC0059462 and NNF21CC0073729) and the Stanford Bio-X Program. The funders had no role in study design, data collection and analysis, decision to publish, or preparation of the manuscript.

1 Goyette, J. & Gaus, K. Mechanisms of protein nanoscale clustering. *Curr Opin Cell Biol* **44**, 86-92 (2017). https://doi.org/10.1016/j.ceb.2016.09.004
2 Toledo, P. L., Gianotti, A. R., Vazquez, D. S. & Ermacora, M. R. Protein nanocondensates: the next frontier. *Biophys Rev* **15**, 515-530 (2023). https://doi.org/10.1007/s12551-023-01105-1
3 Family, F., Meakin, P. & Deutch, J. M. Kinetics of coagulation with fragmentation: Scaling behavior and fluctuations. *Phys Rev Lett* **57**, 727-730 (1986). https://doi.org/10.1103/PhysRevLett.57.727
4 Truong Quang, B. A., Mani, M., Markova, O., Lecuit, T. & Lenne, P. F. Principles of E-cadherin supramolecular organization in vivo. *Curr Biol* **23**, 2197-2207 (2013). https://doi.org/10.1016/j.cub.2013.09.015
5 Benton, R. & St Johnston, D. A conserved oligomerization domain in Bazooka/PAR-3 is important for apical localization and epithelial polarity. *Current Biology* **13**, 1330-1334 (2003). https://doi.org/10.1016/S0960-9822(03)00508-6
6 Lang, C. F., Anneken, A. & Munro, E. M. Oligomerization and feedback on membrane recruitment stabilize PAR-3 asymmetries in C. elegans zygotes. *bioRxiv*, 2023.2008.2004.552031 (2023). https://doi.org/10.1101/2023.08.04.552031
7 Lang, C. F. & Munro, E. M. Oligomerization of peripheral membrane proteins provides tunable control of cell surface polarity. *Biophysical journal* **121**, 4543-4559 (2022). https://doi.org/10.1016/j.bpj.2022.10.035
8 Chae, J. *et al.* The Drosophila tissue polarity gene starry night encodes a member of the protocadherin family. *Development* **126**, 5421-5429 (1999).
9 Usui, T. *et al.* Flamingo, a seven-pass transmembrane cadherin, regulates planar cell polarity under the control of Frizzled. *Cell* **98**, 585-595 (1999).
10 Vinson, C. R. & Adler, P. N. Directional non-cell autonomy and the transmission of polarity information by the *frizzled* gene of *Drosophila*. *Nature* **329**, 549-551 (1987).
11 Vinson, C. R., Conover, S. & Adler, P. N. A *Drosophila* tissue polarity locus encodes a protein containing seven potential transmembrane domains. *Nature* **338**, 263-264 (1989).
12 Taylor, J., Abramova, N., Charlton, J. & Adler, P. N. Van Gogh: a new Drosophila tissue polarity gene. *Genetics* **150**, 199-210 (1998).
13 Wolff, T. & Rubin, G. M. Strabismus, a novel gene that regulates tissue polarity and cell fate decisions in Drosophila. *Development* **125**, 1149-1159 (1998).
14 Klingensmith, J., Nusse, R. & Perrimon, N. The *Drosophila* segment polarity gene dishevelled encodes a novel protein required for response to the wingless signal. *Genes and Development* **8**, 118-130 (1994).
15 Thiesen, H. *et al. dishevelled* is required during *wingless* signaling to establish both cell polarity and cell identity. *Development* **120**, 347-360 (1994).
16 Feiguin, F., Hannus, M., Mlodzik, M. & Eaton, S. The ankyrin repeat protein Diego mediates Frizzled-dependent planar polarization. *Dev Cell* **1**, 93-101. (2001).
17 Gubb, D. *et al.* The balance between isoforms of the prickle LIM domain protein is critical for planar polarity in Drosophila imaginal discs. *Genes Dev* **13**, 2315-2327 (1999).

18 Butler, M. T. & Wallingford, J. B. Planar cell polarity in development and disease. *Nature reviews. Molecular cell biology* **18**, 375-388 (2017). https://doi.org/10.1038/nrm.2017.11
19 Zallen, J. A. Planar polarity and tissue morphogenesis. *Cell* **129**, 1051-1063 (2007).
20 Adler, P. N. & Wallingford, J. B. From Planar Cell Polarity to Ciliogenesis and Back: The Curious Tale of the PPE and CPLANE proteins. *Trends Cell Biol* **27**, 379-390 (2017). https://doi.org/10.1016/j.tcb.2016.12.001
21 Axelrod, J. D. in *Encyclopedia of Cell Biology* Vol. 3 (ed Ralph A. Bradshaw and Philip D. Stahl) 199-207 (Academic Press, 2016).
22 Axelrod, J. D. & Tomlin, C. J. Modeling the control of planar cell polarity. *Wiley Interdiscip Rev Syst Biol Med* **3**, 588-605 (2011). https://doi.org/10.1002/wsbm.138
23 Burak, Y. & Shraiman, B. I. Order and stochastic dynamics in Drosophila planar cell polarity. *PLoS Comput Biol* **5**, e1000628 (2009). https://doi.org/10.1371/journal.pcbi.1000628
24 Schamberg, S., Houston, P., Monk, N. A. & Owen, M. R. Modelling and analysis of planar cell polarity. *Bull Math Biol* **72**, 645-680 (2010). https://doi.org/10.1007/s11538-009-9464-0
25 Semplice, M., Veglio, A., Naldi, G., Serini, G. & Gamba, A. A bistable model of cell polarity. *PLoS One* **7**, e30977 (2012). https://doi.org/10.1371/journal.pone.0030977
26 Cho, B., Pierre-Louis, G., Sagner, A., Eaton, S. & Axelrod, J. D. Clustering and negative feedback by endocytosis in planar cell polarity signaling is modulated by ubiquitinylation of prickle. *PLoS Genet* **11**, e1005259 (2015). https://doi.org/10.1371/journal.pgen.1005259
27 Strutt, H., Warrington, S. J. & Strutt, D. Dynamics of core planar polarity protein turnover and stable assembly into discrete membrane subdomains. *Dev Cell* **20**, 511-525 (2011). https://doi.org/10.1016/j.devcel.2011.03.018
28 Strutt, D. & Strutt, H. Differential activities of the core planar polarity proteins during Drosophila wing patterning. *Dev Biol* **302**, 181-194 (2007).
29 Chen, W. S. *et al.* Asymmetric homotypic interactions of the atypical cadherin flamingo mediate intercellular polarity signaling. *Cell* **133**, 1093-1105 (2008).
30 Lawrence, P. A., Casal, J. & Struhl, G. Cell interactions and planar polarity in the abdominal epidermis of Drosophila. *Development* **131**, 4651-4664 (2004).
31 Struhl, G., Casal, J. & Lawrence, P. A. Dissecting the molecular bridges that mediate the function of Frizzled in planar cell polarity. *Development* **139**, 3665-3674 (2012). https://doi.org/10.1242/dev.083550
32 Strutt, H. & Strutt, D. Differential stability of flamingo protein complexes underlies the establishment of planar polarity. *Curr Biol* **18**, 1555-1564 (2008). https://doi.org/10.1016/j.cub.2008.08.063
33 Tree, D. R. *et al.* Prickle mediates feedback amplification to generate asymmetric planar cell polarity signaling. *Cell* **109**, 371-381 (2002). https://doi.org/10.1016/S0092-8674(02)00715-8
34 Bastock, R., Strutt, H. & Strutt, D. Strabismus is asymmetrically localised and binds to Prickle and Dishevelled during Drosophila planar polarity patterning. *Development* **130**, 3007-3014 (2003).

35 Kan, W. *et al.* Limited dishevelled/Axin oligomerization determines efficiency of Wnt/beta-catenin signal transduction. *eLife* **9** (2020). https://doi.org/10.7554/eLife.55015
36 Ayukawa, T. *et al.* Dachsous-dependent asymmetric localization of spiny-legs determines planar cell polarity orientation in Drosophila. *Cell reports* **8**, 610-621 (2014). https://doi.org/10.1016/j.celrep.2014.06.009
37 Strutt, H., Gamage, J. & Strutt, D. Reciprocal action of Casein Kinase Iepsilon on core planar polarity proteins regulates clustering and asymmetric localisation. *eLife* **8** (2019). https://doi.org/10.7554/eLife.45107
38 Jenny, A., Darken, R. S., Wilson, P. A. & Mlodzik, M. Prickle and Strabismus form a functional complex to generate a correct axis during planar cell polarity signaling. *Embo J* **22**, 4409-4420 (2003).
39 Devenport, D. & Fuchs, E. Planar polarization in embryonic epidermis orchestrates global asymmetric morphogenesis of hair follicles. *Nature Cell Biology* (2008).
40 Curtin, J. A. *et al.* Mutation of Celsr1 disrupts planar polarity of inner ear hair cells and causes severe neural tube defects in the mouse. *Curr Biol* **13**, 1129-1133 (2003).
41 Stahley, S. N., Basta, L. P., Sharan, R. & Devenport, D. Celsr1 adhesive interactions mediate the asymmetric organization of planar polarity complexes. *eLife* **10** (2021). https://doi.org/10.7554/eLife.62097
42 Strutt, H., Gamage, J. & Strutt, D. Robust Asymmetric Localization of Planar Polarity Proteins Is Associated with Organization into Signalosome-like Domains of Variable Stoichiometry. *Cell reports* **17**, 2660-2671 (2016). https://doi.org/10.1016/j.celrep.2016.11.021
43 Weiner, A. T., Cho, B., Suyama, K. & Axelrod, J. D. Cell autonomous polarization by the planar cell polarity signaling pathway. *bioRxiv* (2023). https://doi.org/10.1101/2023.09.26.559449
44 Leckband, D. Cell adhesion: sizing up a sticky situation. *Curr Biol* **23**, R1008-R1011 (2013). https://doi.org/10.1016/j.cub.2013.10.018
45 De Greef, T. F. A. *et al.* Supramolecular Polymerization. *Chemical Reviews* **109**, 5687-5754 (2009). https://doi.org/10.1021/cr900181u
46 Singh, A. *et al.* Polarized microtubule dynamics directs cell mechanics and coordinates forces during epithelial morphogenesis. *Nat Cell Biol* **20**, 1126-1133 (2018). https://doi.org/10.1038/s41556-018-0193-1
47 Warrington, S. J., Strutt, H., Fisher, K. H. & Strutt, D. A Dual Function for Prickle in Regulating Frizzled Stability during Feedback-Dependent Amplification of Planar Polarity. *Curr Biol* **27**, 2784-2797 e2783 (2017). https://doi.org/10.1016/j.cub.2017.08.016
48 Liu, Y. T. *et al.* Molecular basis of Wnt activation via the DIX domain protein Ccd1. *J Biol Chem* **286**, 8597-8608 (2011). https://doi.org/10.1074/jbc.M110.186742
49 Bienz, M. Signalosome assembly by domains undergoing dynamic head-to-tail polymerization. *Trends Biochem Sci* **39**, 487-495 (2014). https://doi.org/10.1016/j.tibs.2014.08.006

50 Axelrod, J. D. in *Encyclopedia of Cell Biology (Second Edition)* (eds Ralph A. Bradshaw, Gerald W. Hart, & Philip D. Stahl) 233-242 (Academic Press, 2023).
51 Shimada, Y., Yonemura, S., Ohkura, H., Strutt, D. & Uemura, T. Polarized Transport of Frizzled along the Planar Microtubule Arrays in Drosophila Wing Epithelium. *Dev Cell* **10**, 209-222 (2006).
52 Olofsson, J., Sharp, K. A., Matis, M., Cho, B. & Axelrod, J. D. Prickle/spiny-legs isoforms control the polarity of the apical microtubule network in planar cell polarity. *Development* **141**, 2866-2874 (2014). https://doi.org/10.1242/dev.105932
53 Matis, M., Russler-Germain, D. A., Hu, Q., Tomlin, C. J. & Axelrod, J. D. Microtubules provide directional information for core PCP function. *eLife* **3**, e02893 (2014). https://doi.org/10.7554/eLife.02893
54 Mohapatra, L., Goode, B. L., Jelenkovic, P., Phillips, R. & Kondev, J. Design Principles of Length Control of Cytoskeletal Structures. *Annual Review of Biophysics* **45**, 85-116 (2016). https://doi.org/https://doi.org/10.1146/annurev-biophys-070915-094206
55 Edelstein-Keshet, L. & Ermentrout, G. B. Models for the length distributions of actin filaments: I. Simple polymerization and fragmentation. *Bulletin of Mathematical Biology* **60**, 449-475 (1998). https://doi.org/10.1006/bulm.1997.0011
56 Lee, D. S. W. *et al.* Size distributions of intracellular condensates reflect competition between coalescence and nucleation. *Nature Physics* **19**, 586-596 (2023). https://doi.org/10.1038/s41567-022-01917-0
57 Olofsson, J. & Axelrod, J. D. Methods for studying planar cell polarity. *Methods* **68**, 97-104 (2014). https://doi.org/10.1016/j.ymeth.2014.03.017
58 Classen, A. K., Aigouy, B., Giangrande, A. & Eaton, S. Imaging Drosophila pupal wing morphogenesis. *Methods Mol Biol* **420**, 265-275 (2008). https://doi.org/10.1007/978-1-59745-583-1_16
59 Chang, A. C. *et al.* Single Molecule Force Measurements in Living Cells Reveal a Minimally Tensioned Integrin State. *ACS Nano* **10**, 10745-10752 (2016). https://doi.org/10.1021/acsnano.6b03314
60 Tan, S. J. *et al.* Regulation and dynamics of force transmission at individual cell-matrix adhesion bonds. *Sci Adv* **6**, eaax0317 (2020). https://doi.org/10.1126/sciadv.aax0317
61 Edelstein, A. D. *et al.* Advanced methods of microscope control using muManager software. *J Biol Methods* **1** (2014). https://doi.org/10.14440/jbm.2014.36
62 Schindelin, J. *et al.* Fiji: an open-source platform for biological-image analysis. *Nat Methods* **9**, 676-682 (2012). https://doi.org/10.1038/nmeth.2019
63 Culley, S., Tosheva, K. L., Matos Pereira, P. & Henriques, R. SRRF: Universal live-cell super-resolution microscopy. *Int J Biochem Cell Biol* **101**, 74-79 (2018). https://doi.org/10.1016/j.biocel.2018.05.014
64 Leake, M. C. *et al.* Stoichiometry and turnover in single, functioning membrane protein complexes. *Nature* **443**, 355-358 (2006). https://doi.org/10.1038/nature05135

65 Lenn, T. *et al*. Measuring the stoichiometry of functional PspA complexes in living bacterial cells by single molecule photobleaching. *Chem Commun (Camb)* **47**, 400-402 (2011). https://doi.org/10.1039/c0cc01707h

66 Lowe, A. R. *et al*. Importin-beta modulates the permeability of the nuclear pore complex in a Ran-dependent manner. *eLife* **4** (2015). https://doi.org/10.7554/eLife.04052

67 Axelrod, J. D. Unipolar membrane association of Dishevelled mediates Frizzled planar cell polarity signaling. *Genes Dev* **15**, 1182-1187. (2001).

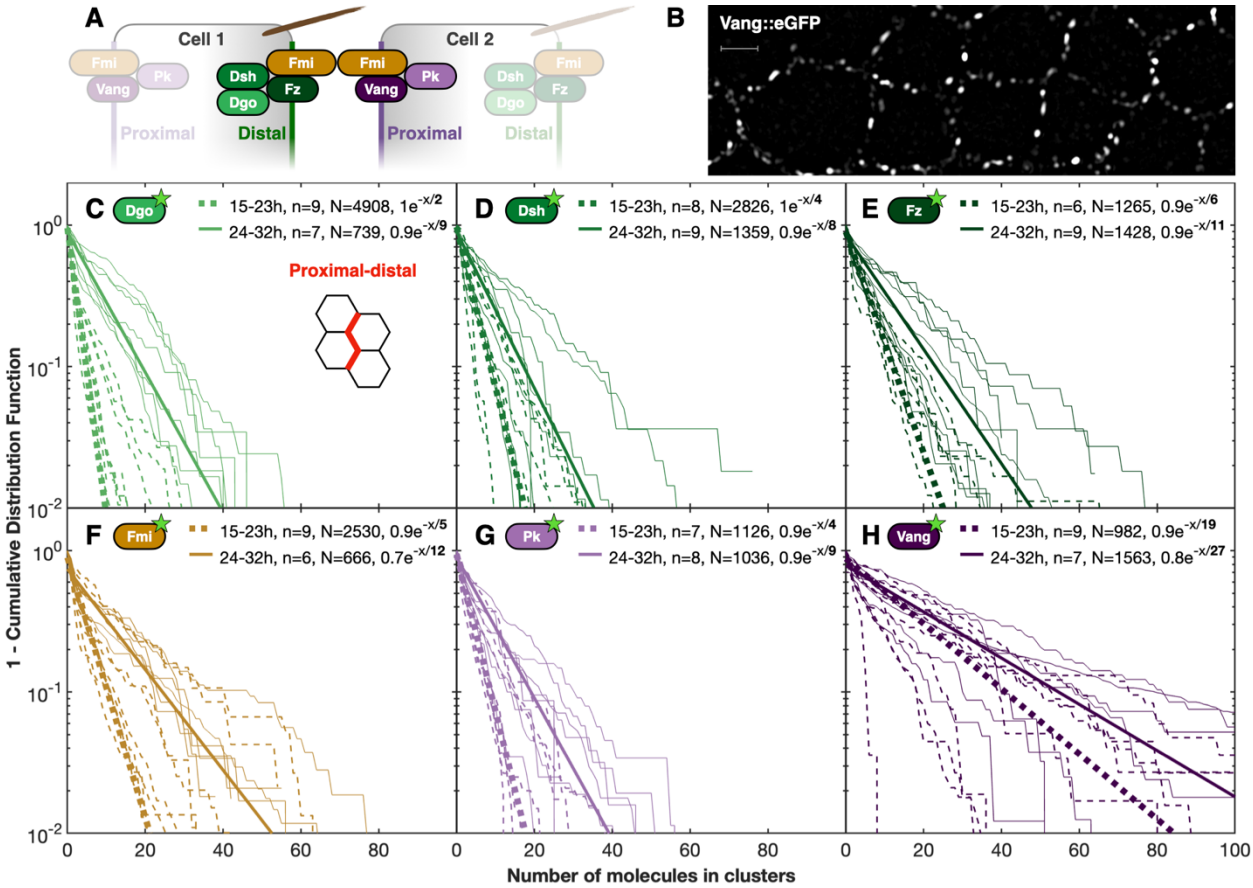

Figure 1: Numbers of core component molecules in PCP clusters follow single exponential distributions. (A) Cartoon of a PCP signaling cluster. The distal subcomplex consists of Diego (Dgo), Dishevelled (Dsh), and Frizzled (Fz). The proximal subcomplex consists of Prickle (Pk) and Van Gogh (Vang). Flamingo (Fmi) is in both subcomplexes and connects them across intercellular junctions. **(B)** High-resolution image of Vang::eGFP acquired with Total Internal Reflection Fluorescence (TIRF) Microscopy (see *Methods* for details). Note how Vang assembles into clusters of varying sizes along cell-cell junctions. Scale bar is 2 µm. **(C-H)** Cluster size distributions of **(C)** Dgo, **(D)** Dsh, **(E)** Fz, **(F)** Fmi, **(G)** Pk, and **(H)** Vang (each tagged with GFP), grouped into an early age group (15-23h, after puparium formation, APF, dashed lines) and a late age group (24-32h APF, solid lines) gated on proximal-distal boundaries. Thin lines indicate individual samples (wings). Solid lines illustrate a single exponential fit through a median wing. *n* indicates the number of wings imaged, *N* indicates the total number of clusters measured, Note the logarithmic *y*-axis. The average number of each component in clusters can be read as the denominator of the exponent. For anterior-posterior boundaries, see Figure S1.

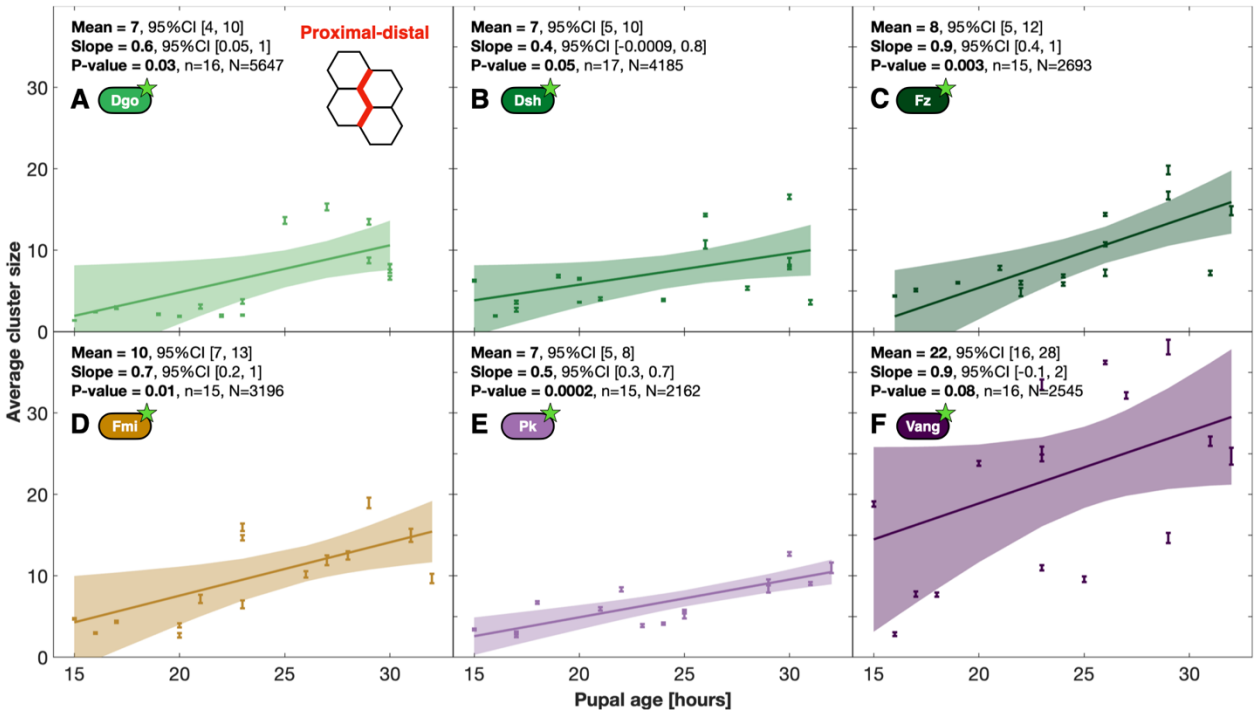

Figure 2: PCP clusters grow and cluster stoichiometry is maintained. (A-F) The average number of monomers in clusters along proximal-distal boundaries as a function of the number of hours APF for **(A)** Dgo, **(B)** Dsh, **(C)** Fz, **(D)** Fmi, **(E)** Pk, and **(F)** Vang. Each dot represents a single-exponential fit through the cluster size distribution found in one sample and the error bar represents the standard error of the estimate (see Figure 1). For each core protein, a weighted linear regression model is shown through all samples (solid line) with 95% confidence interval (CI, dashed lines). The mean indicates the average cluster size at 23.5 hours APF, and the slope represents the rate of increase in monomers/hour. The P-value tests the significance of the slope (see *Methods*). *n* is the number of biological samples, and *N* is the total number of clusters analyzed. For anterior-posterior boundaries, see Figure S2.

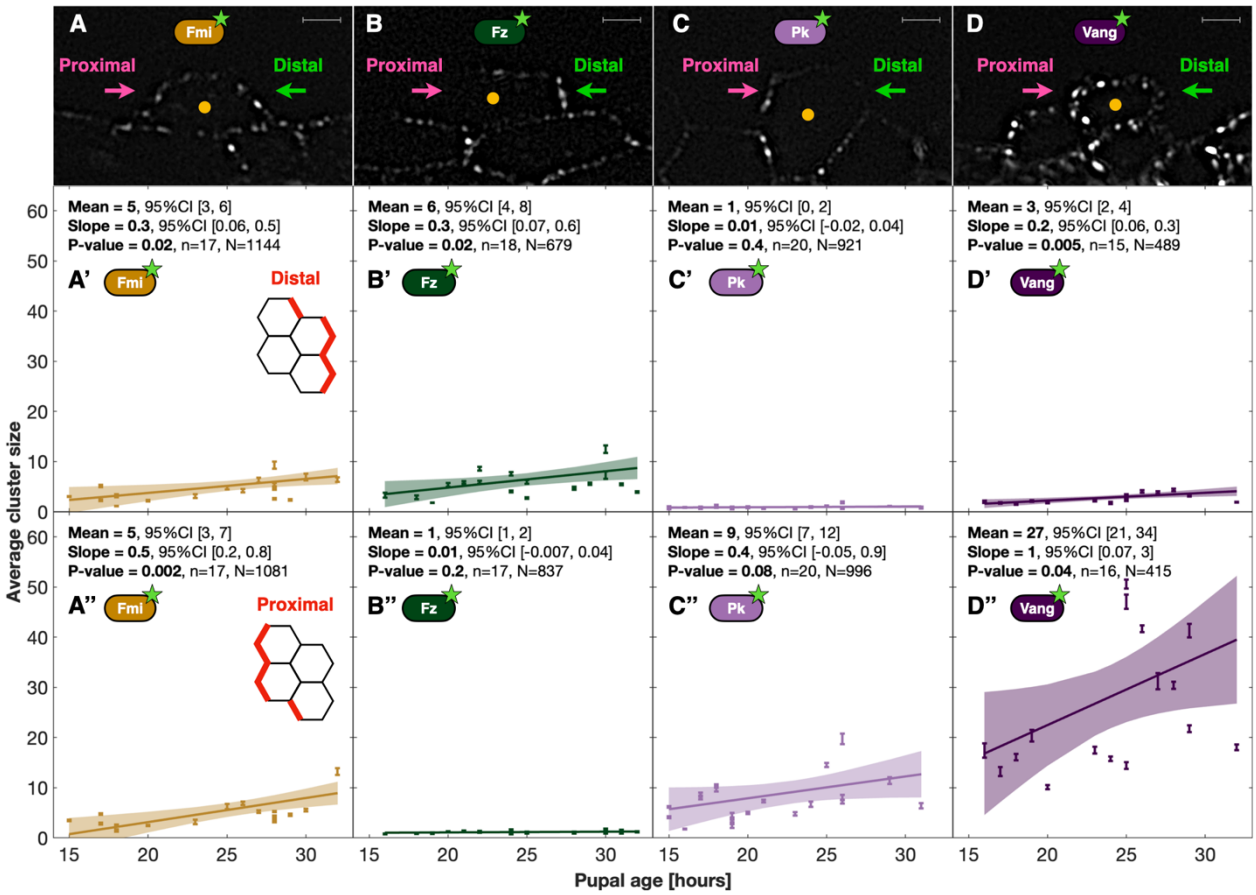

Figure 3: PCP protein polarization assayed by clonal analysis. (A-D) High-resolution image of **(A)** Fmi, **(B)** Fz, **(C)** Pk, (**D)** Vang, each expressed mosaically, all tagged with eGFP (see *Methods* for details). Orange dots indicate cell centers. All scale bars are 2 µm. The apparent paucity of Fz clusters on the proximal side and Pk clusters on the distal side is likely due to smaller clusters not being readily apparent in these processed images. In contrast, note the presence of visible distal Vang subcomplexes. **(A'-D'')** The average number of monomers in clusters based on single exponential fits through the cluster size distribution identified in individual samples (dots and error bars). **(A'-D')** Clusters along distal cell boundaries vs. along **(A''-D'')** proximal cell boundaries. (**A', A'')** Fmi. **(B', B'')** Fz. **(C', C'')** Pk. **(D', D'')** Vang. Note the presence of Fmi on both proximal and distal sides. Dots, error bars, Mean, Slope, P-value, *n* and *N* as in Figure 2. The underlying cluster size distributions are shown in Figure S3. For anterior-posterior boundaries, see Figure S2.

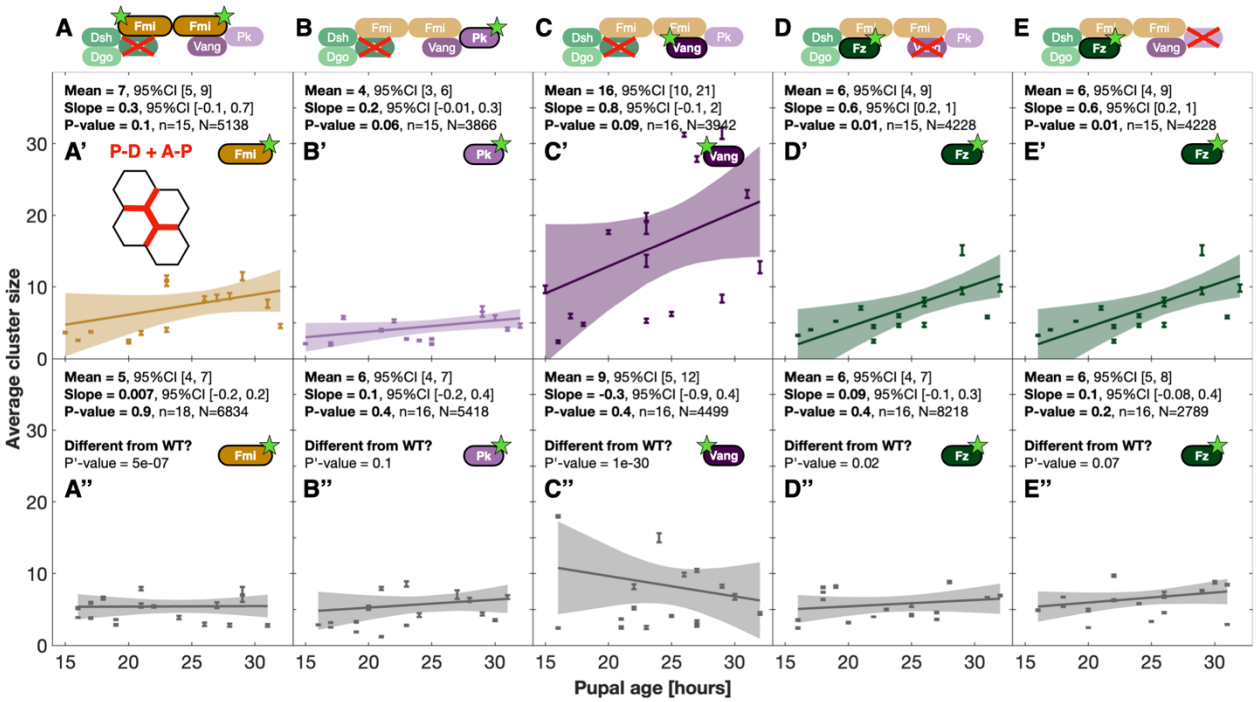

Figure 4: PCP clusters form in null mutants. (A-E) Schematic of the loss-of-function experiments. **(A'-E'')** Cluster size distributions in wild-type (colored, **A'-E'**) compared to mutant conditions (gray, **A''-E''**), when examining all cell boundaries. **(A'-E')** Wild type data similar to the sum of Figures 2 and S2. **(A')** Fmi::eGFP, **(B')** Pk:eGFP, **(C')** Vang::eGFP **(D')** Fz::eGFP **(E')** Identical to (D) **(A''-E'')** Loss-of-function data including all cell boundaries. **(A'')** Fmi::eGFP in fz^{R52}/fz^{R52}, **(B'')** Pk::eGFP in fz^{R52}/fz^{R52}, **(C'')** Vang::eGFP in fz^{R52}/fz^{R52}, **(D'')** Fz::eGFP in $vang^{stbm6}/vang^{stbm6}$, **(E'')** Fz::eGFP in $pk^{pk\text{-}sple13}/pk^{pk\text{-}sple13}$. Note that differences in cluster sizes are most pronounced in wild type late pupal ages, whereas little difference is found between wild type and mutant condition at earlier pupal ages. Dots, error bars, Mean, Slope, P-value, *n* and *N* as in Figure 2. P' = significance of the difference between loss-of-function and corresponding wild type conditions by linear mixed model test. For sample images of the loss-of-function conditions, see Figure S4.

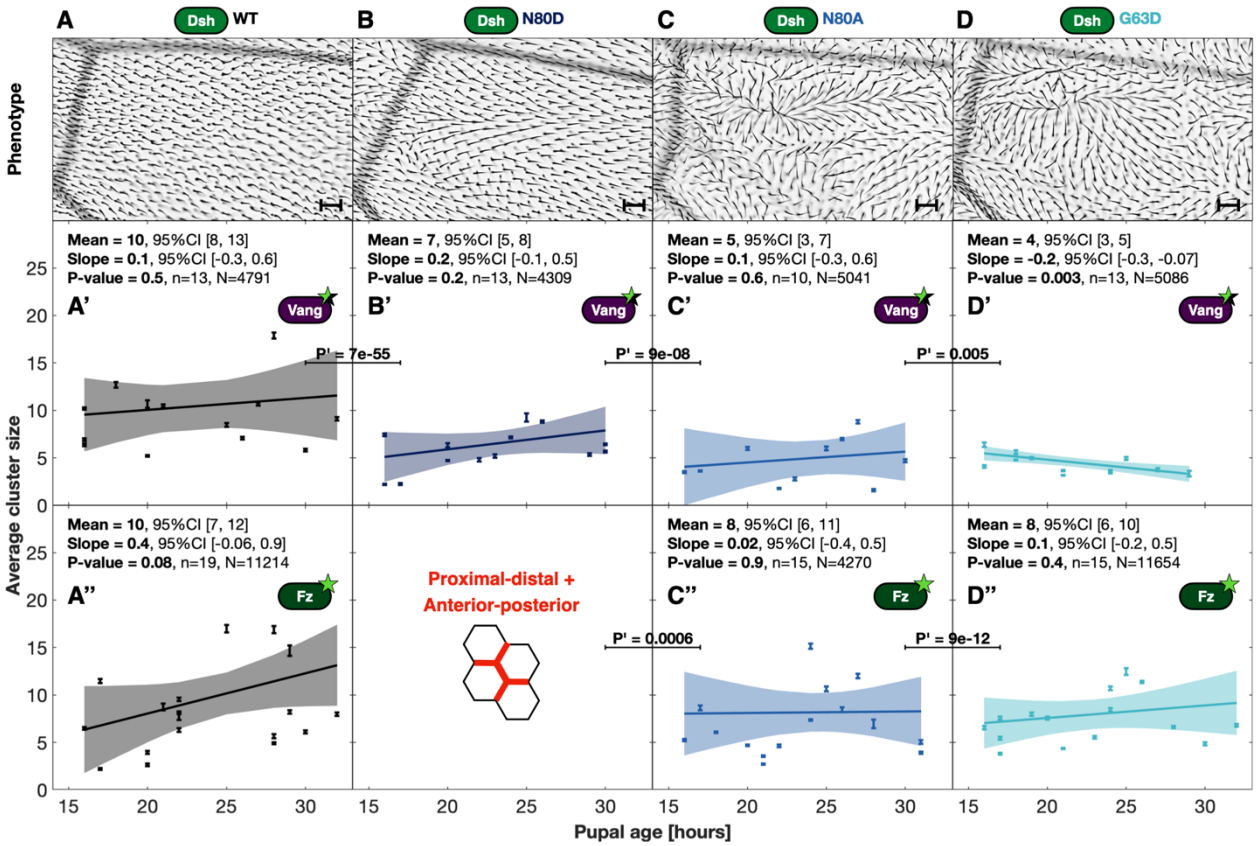

Figure 5: Growth of larger clusters is required for downstream polarity readout. (A-D) Trichome polarity patterns on the adult *Drosophila* wings near the posterior crossvein in hemizygous males expressing wild type or DIX mutant Dsh from a transgene on a *dsh*^{v26} (null) chromosome: **(A)** Wild type (WT, control), **(B)** Dsh^{N80D}, **(C)** Dsh^{N80A}, **(D)** Dsh^{G63D}. All scale bars are 20 µm. **(A'-D')** The average number of heterozygous tagged Vang::eGFP monomers in clusters along the entire cell periphery in the **(A')** WT (control), (B') Dsh^{N80D} **(C')** Dsh^{N80A}, and (**D'**) Dsh^{G63D} conditions. **(A''-D'')** The average number of homozygously tagged Fz::eGFP monomers in **(A'')** WT (control), **(C'')** Dsh^{N80A}, and (**D'')** Dsh^{G63D} conditions. This experiment was not performed for Dsh^{N80D}. Note the severity of the hair polarity phenotype correlates with reduced cluster sizes for Vang, and to a lesser extent, Fz. **(A'-D'')**. Growth of Fz in WT **(A'')** might be expected, but because we are combining measures of proximal-distal where growth is significant (Figure 2) and anterior-posterior junctions, where it is not significant (Figure S2), significance is not reached here. Dots, error bars, Mean, Slope, P-value, *n* and *N* as in Figure 2. P' = significance of the difference between two conditions by linear mixed model test (C'' compares to A'').

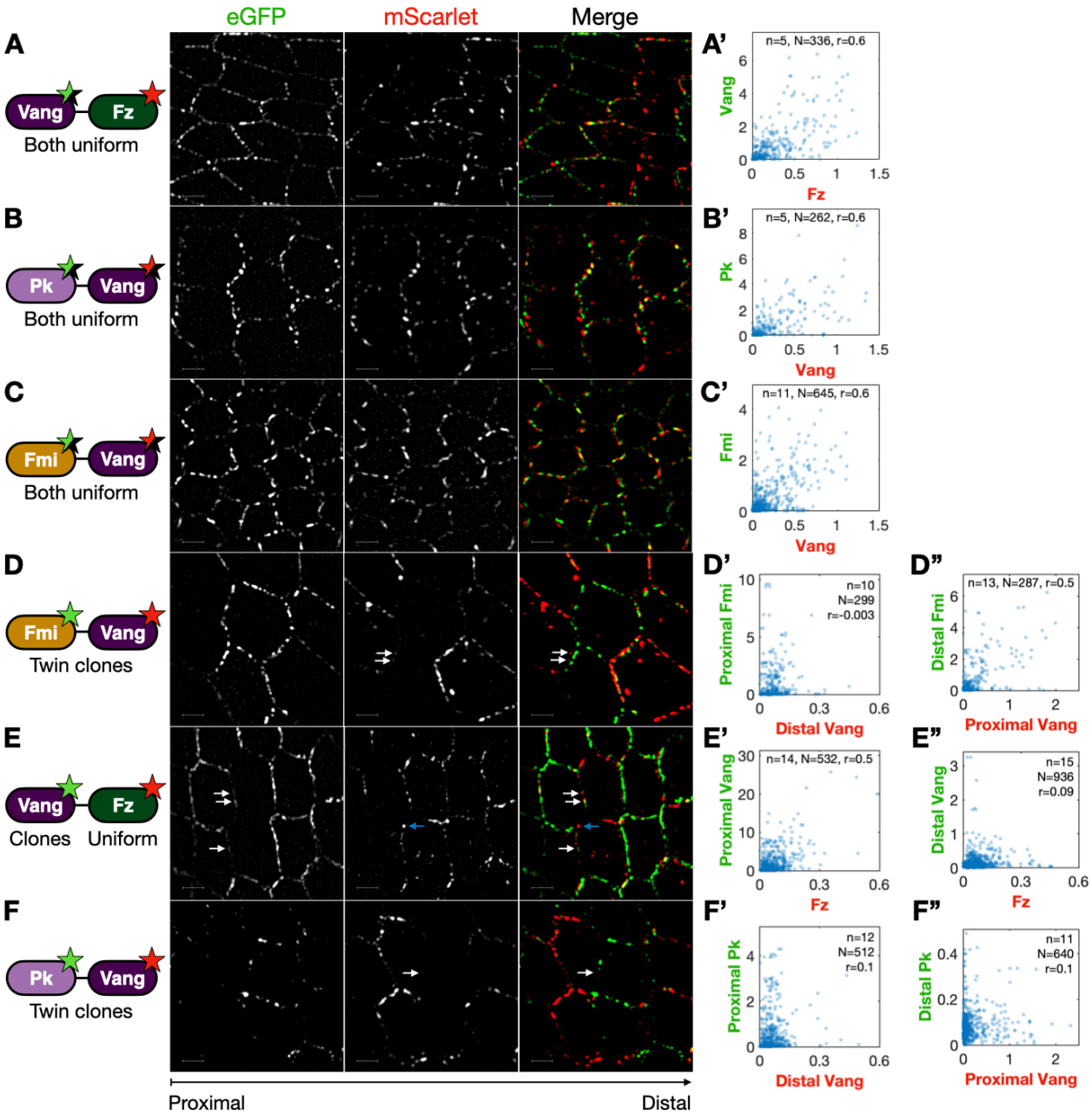

Figure 6: Two-color imaging reveals that large clusters are more likely to be oriented correctly. (A-C) Processed TIRF microscopy sample images of uniform expression of **(A)** heterozygous Vang::eGFP, homozygous Fz::mScarlet, **(B)** heterozygous Pk::eGFP, heterozygous mScarlet::Vang, and **(C)** heterozygous Fmi::eGFP, heterozygous mScarlet::Vang. **(A'-C')** Analyzed intensities at paired clusters along proximal-distal boundaries (details: see Methods). Each blue dot represents one (light blue) or more (dark blue) clusters. **(D)** Twin clones of Fmi::eGFP, mScarlet::Vang. **(E)** Clones of Vang::eGFP in a uniform Fz::mScarlet background. **(F)** Twin clones of Pk::eGFP, mScarlet::Vang. Analyzed intensities at paired clusters along proximal or distal boundaries as labeled: **(D')** Proximal Fmi vs. distal Vang. **(D'')** Distal Fmi vs. proximal Vang. **(E')** Proximal Vang vs. uniform Fz. **(E'')** Distal Vang vs. uniform Fz. **(F')** Proximal Pk vs. distal Vang. **(F'')** Distal Pk vs. proximal Vang. *n* is the number of wings imaged. *N* is the total number of paired clusters analyzed. *r* is the correlation coefficient. All two-

color wings imaged 27 hr ± 3 hr after puparium formation. White arrows point at examples of distal Vang. Blue arrow points to an example of strong Fz signal without detectable distal Vang. Note, the varying *x*- and *y*-scales, and the asymmetry degree of Vang and Pk, matches the one found in Figure 3. All scale bars are 2 μm. For anterior-posterior boundaries, see Figure S5.

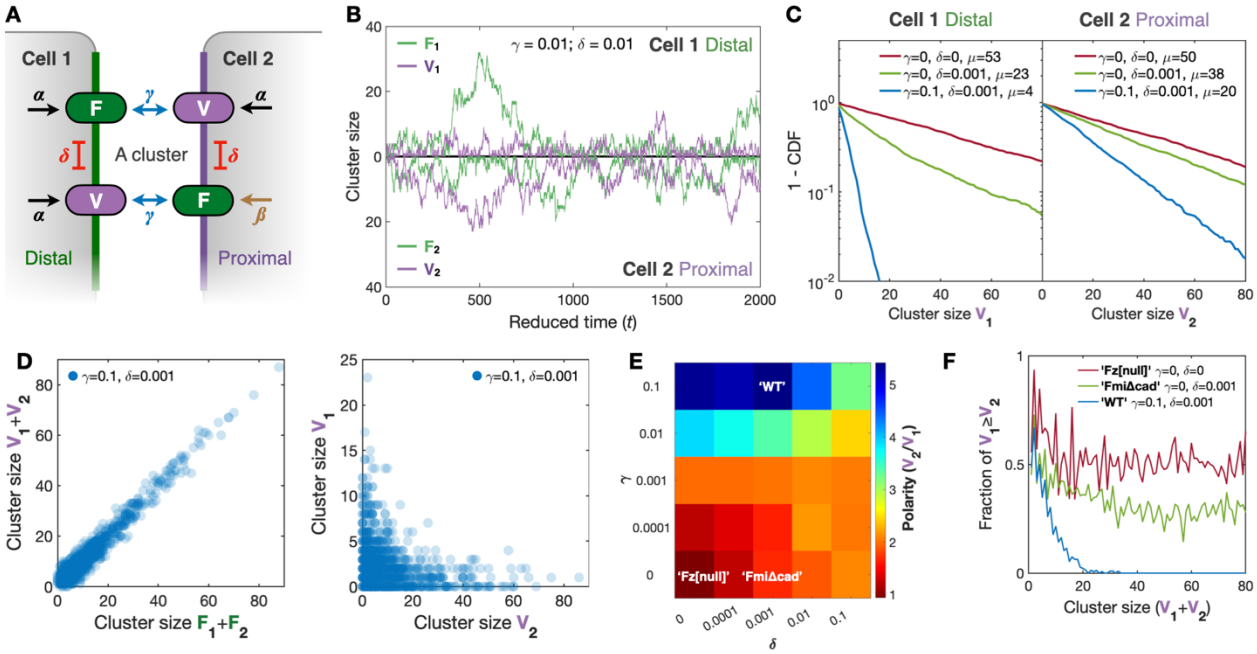

Figure 7: Mathematical model of planar cell polarity (PCP) cluster formation. (A) Schematic (see *Methods* for details) **(B)** Example run illustrating how monomers stochastically enter and leave the cluster as a function of time (step number). **(C)** Single exponential cluster size distributions for selected parameters. V_2 indicates subcomplex V in cell 2, and V_1 indicates subcomplex V in cell 1. μ is the average cluster size. **(D)** Two-color simulations. Compare the left panel (V_1+V_2 *vs* F_1+F_2) to Figure 6A'-C') and the right panel (V_1 *vs* V_2) to Figure 6D'' and E'. **(E)** Phase diagram. **(F)** Fraction of incorrectly oriented clusters as a function of cluster size. **(C-F)** Throughout the figure, the number of simulated clusters N = 1000, the measurements occur at time $T = 10^6$, the basal influx α = 0.495 and the biased influx β = 0.4, blue mimics wild type with intercellular binding strength γ = 0.1 and intracellular inhibition strength δ = 0.001, green mimics FmiΔcad with δ = 0.001 and γ = 0, and red mimics loss-of-function e.g. fz[null] with $\gamma = \delta$ = 0. For model variations and parameter scans, see the Appendix and Figures S6-S8.